Bond-order potentials for the Ti_3AlC_2 and Ti_3SiC_2 MAX phases

Gabriel Plummer and Garritt J. Tucker*
Department of Mechanical Engineering, Colorado School of Mines, Golden, Colorado 80401, USA

(Received 27 September 2019; revised manuscript received 22 November 2019; published 18 December 2019)

Bond-order potentials have been developed for the Ti_3AlC_2 and Ti_3SiC_2 MAX phases within the Tersoff formalism. Parameters were determined by independently considering each interatomic interaction present in the system and fitting them to the relevant structural, elastic, and defect properties for a number of unary, binary, and ternary structures. A number of material properties, including those not used in the fitting procedure, are reproduced with a high degree of accuracy when compared to experiment and *ab initio* calculations. Additionally, well-documented MAX phase behaviors such as plastic anisotropy and kinking nonlinear elasticity are demonstrated to be captured by the potentials. As a first highly accurate atomistic model for MAX phases, these potentials provide the opportunity to study some of the fundamental mechanisms behind unique MAX phase properties. Additionally, the fitting procedure employed is highly transferable and should be applicable to numerous other MAX phases.

DOI: 10.1103/PhysRevB.100.214114

I. INTRODUCTION

MAX phases are ternary metal carbides and nitrides with the general formula $M_{n+1}AX_n$, where $n = 1$, 2, or 3, M is an early transition metal, A is an A-group element, and X is C and/or N. They represent a unique class of layered materials, where close-packed $M_{n+1}X_n$ layers are interleaved with pure A layers (Fig. 1). The thickness of the MX layers is determined by n, and therefore MAX phases are classified into three categories accordingly: 211, 312, or 413 (i.e. M_2AX, M_3AX_2, and M_4AX_3, respectively). MAX phases can be formed from a wide range of M and A elements, with 60+ compounds being synthesized to date [1]. The layered structure, made up of strong M-X bonds and relatively weak M-A bonds, imparts a unique combination of properties; they share many advantageous properties of their corresponding binary metal carbides and nitrides such as high elastic stiffness, good electrical and thermal conductivity, and high temperature stability, however, they are also readily machinable, relatively soft, resistant to thermal shock, and damage tolerant [2–4]. As a result, MAX phases have been proposed for a wide range of uses, including high temperature structural applications [5], protective coatings [6,7], electrical contacts [8], nuclear fuel cladding [9], and more.

While MAX phases are already being implemented in many applications, the fundamental mechanisms behind a number of their interesting properties, which have made them the subject of such intensive study over the past two decades, remain largely unknown. This limits the degree to which they can be better engineered for specific applications. A prime example is their well-documented kinking nonlinear elastic (KNE) behavior [1,3]. When polycrystalline samples are loaded in compression or single crystals are nanoindented, MAX phases exhibit fully and spontaneously reversible stress-strain hysteresis loops. The energy dissipated is due to the formation of kink bands, a common deformation mode in layered solids [10]. The micromechanism responsible for the formation of kink bands has long been hypothesized to be basal dislocation arrays [10–12], however, recent observations have provided evidence for a different micromechanism at work, atomic scale buckling of layers termed *ripplocations* [13–16]. Another example is the remarkable radiation tolerance of MAX phases, as neutron studies suggest nearly all irradiation-induced damage disappears above 700 °C [17,18]. These notable observations have been ascribed to the ability of A layers to act as efficient defect sinks and migration pathways, but the underlying defect processes by which this occurs remain unknown. The phenomena associated with KNE behavior and radiation tolerance occur on time scales much too short to observe directly via experiment and on length scales beyond the capabilities of density functional theory (DFT) calculations. Atomistic simulations employing an interatomic potential provide a middle ground, in which these important mechanisms and a variety of others can be studied directly, provided an appropriate interatomic potential is defined.

There is a clear need for atomistic modeling of MAX phases, but research activity in developing an accurate interatomic potential has been minimal. Presently, only one interatomic potential has been developed for a MAX phase [19]; it was used to study $Ti_2AlN/TiAl$ composites but focus was placed on interfacial properties and not on extensive validation showing that it can reproduce fundamental MAX phase behaviors. The difficulty in developing interatomic potentials for MAX phases arises from the complexity of the system—ternary systems have significantly more interactions to account for than unary or binary ones—and its heterogeneity—M, A, and X elements can be significantly different in how they interact with themselves and one another. The goal of this study is to overcome these challenges by using a flexible potential form combined with a stepwise

*Corresponding author: tucker@mines.edu

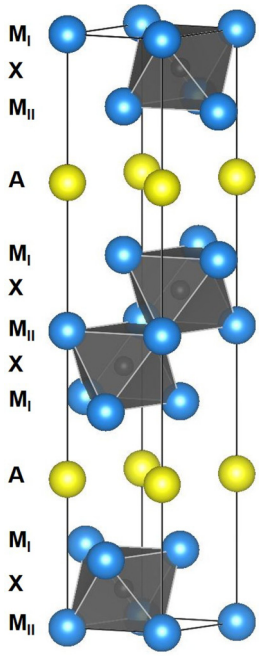

FIG. 1. A representative unit cell of the 312 MAX phases, where the M, A, and X layers are labeled, and atoms are colored blue, yellow, and gray, respectively. Additionally, the M_6X octahedral units are shown.

fitting procedure to produce accurate MAX phase interatomic potentials. The 312 MAX phases, Ti_3AlC_2 and Ti_3SiC_2, were chosen as they are some of the most widely studied and thus significant experimental/DFT data is available to use for fitting and validation. The methodology utilized herein should be capable of being transferred to other MAX phases as well, provided the necessary data is available.

II. POTENTIAL FORM

MAX phases are known to possess a combination of ionic, covalent, and metallic bonding [4]. Therefore, any potential form must be flexible enough to handle this diverse set of interactions, while maintaining a sufficient degree of simplicity so that simulations may be appropriately scaled. The bond-order potential (BOP) as originally proposed by Tersoff [20] along with minor variants has proven to accurately describe a number of systems encompassing covalent [21,22], metallic [23–26], and mixed ionic/covalent bonding [27–29]. Combined with its simplicity compared to more complex bond-order [30,31] and reactive potentials [32,33], it is an ideal candidate for modeling MAX phases. The modified embedded atom method (MEAM) [34] was also considered but ultimately not chosen as it imposes more restrictions on the types of structures it can model.

The formalism used herein is described in detail in Ref. [27], but briefly the energy functional takes the following form:

$$E = \frac{1}{2}\sum_i \sum_{i\neq j} f_C(r_{ij})[f_R(r_{ij}) + b_{ij} f_A(r_{ij})] \tag{1}$$

where f_C is a cutoff function, f_R and f_A represent repulsive and attractive two-body terms respectively, and b_{ij} is a many-body term called the bond-order parameter, which accounts for angular dependence of bonds and couples coordination number to bond strength. The smooth cutoff function is defined by the following with free parameters R and D:

$$f_C(r_{ij}) = \begin{cases} 1 & r_{ij} < R - D \\ \frac{1}{2} - \frac{1}{2}\sin\left(\frac{\pi}{2}\frac{r_{ij}-R}{D}\right) & R - D < r_{ij} < R + D \\ 0 & r_{ij} > R + D \end{cases} \tag{2}$$

Typically, R and D are defined such that only first nearest neighbors fall within the cutoff range. The two-body terms are taken as Morse potentials with the free parameters A, λ_1, B, and λ_2:

$$f_R(r_{ij}) = A\exp(-\lambda_1 r_{ij}) \tag{3}$$

$$f_A(r_{ij}) = -B\exp(-\lambda_2 r_{ij}) \tag{4}$$

The bond-order term is given by

$$b_{ij} = (1 + \zeta_{ij})^{-\frac{1}{2}} \tag{5}$$

$$\zeta_{ij} = \sum_{k\neq i,j} f_C(r_{ik}) g(\theta_{ijk}) \exp[\lambda_3(r_{ij} - r_{ik})] \tag{6}$$

$$g(\theta_{ijk}) = \gamma\left(1 + \frac{c^2}{d^2} - \frac{c^2}{d^2 + (\cos\theta_{ijk} - h)^2}\right) \tag{7}$$

where λ_3, γ, c, d, and h are free parameters. This amounts to 11 free parameters per elemental interaction, 14 per binary interaction, and 3 additional ternary parameters. In total, a ternary potential employing this form requires 78 free parameters to be fitted.

III. FITTING PROCEDURE

Fitting such a large number of free parameters simultaneously presents a formidable optimization problem, especially when the objective function does not have an analytical form as in atomistic simulations. To circumvent this difficulty, most binary and ternary interatomic potentials are fitted by considering each interaction independently. This stepwise approach has proven to be successful for previous ternary potentials developed within the bond-order formalism used herein [24,26]. As such, elemental interactions (Ti-Ti and Al-Al) were first fitted to properties of the corresponding elemental phases (previously published C-C and Si-Si interaction parameters were already available [21]). Next, the binary interaction Ti-C was fitted to properties of bulk TiC, as the MX layers in MAX phases adopt a similar rocksalt configuration. Finally, the binary interactions Ti-A (A = Al or Si) and A-C were fitted to MAX phase properties along with the three additional ternary parameters. The A-C interactions do not contribute in the equilibrium MAX phase structure, so they were fitted after the Ti-A interactions to a number of defect-containing structures. This stepwise approach is illustrated in Fig. 2. Thus the original, highly complex optimization problem was broken down into a number of more tractable ones, limiting the number of parameters fitted simultaneously to 17 at most.

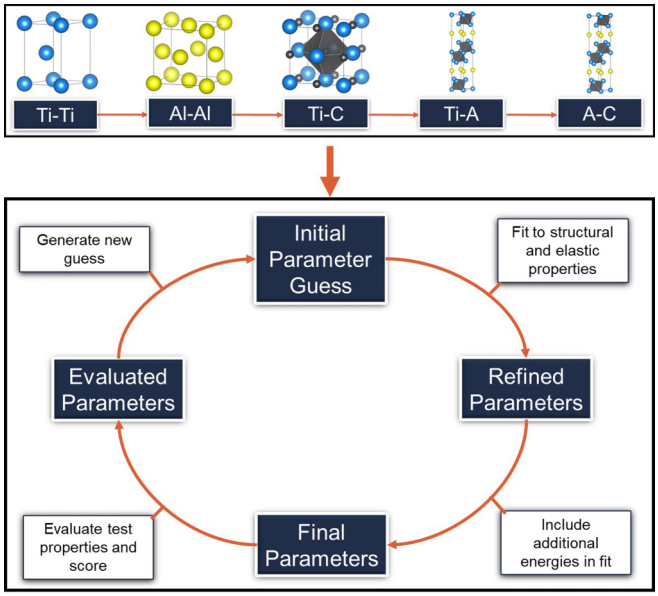

FIG. 2. A flowchart illustrating the workflow utilized to develop the MAX phase potentials and the fitting procedure used for each interaction.

Each interaction was fitted by minimizing the sum of squared residuals for a number of relevant material properties, utilizing a simplex search method [35]. The residuals were normalized by a tolerance value according to their units. Typical tolerance values used were 0.03 Å, 5 GPa, and 0.1 eV. This form of objective function contains a large number of local minima, making the initial parameter guess of great importance for the final result. Due to this, an iterative fitting approach was taken in which a large number of initializations (on the order of 10^2–10^3) were generated and subsequently optimized in an attempt to best approach a global minimum (see flowchart in Fig. 2). Each initialization was generated randomly from a range of parameter values informed by previous published potentials and, once they were completed, the elemental interaction parameters developed herein. Within each iteration, two separate phases of optimization were performed as it was found to be more efficient than a single optimization. The first phase, a rough optimization, involved fitting to structural properties such as lattice constants and formation energy as well as elastic properties. The second phase, a more stringent optimization, then included other energies such as structural transitions and point defect formations. Once an iteration was completed, the final parameter set was validated against a set of test properties not included in the fitting scheme. These included additional structural transitions, point defect formation energies, and surface energies. Finalized parameter sets for each interaction were chosen after comparing both fitted and test properties across each iteration. All calculations of properties during the fitting procedure were performed within LAMMPS, the Large-scale Atomic/Molecular Massively Parallel Simulator (lammps.sandia.gov), an open source molecular dynamics (MD) code [36]. Visualizations of atomistic simulations were created with the open source software OVITO [37].

TABLE I. Calculated properties of Ti using the BOP in comparison with experimental and DFT data. Properties calculated with a MEAM potential [38] are also presented for comparison. Properties marked with an asterisk (*) were fitted to, while all others were used for validation. Properties listed are lattice constants (a, c), cohesive energy (E_c), elastic constants (C_{ij}), structural energy differences (ΔE), vacancy formation energy (V_{Ti}), octahedral and basal octahedral interstitial formation energies (Ti_O, Ti_{BO}), surface energies (E_{surf}), stacking fault energy (E^{sf}), linear thermal expansion coefficient (α), specific heat (C_P), and melting point (T_m).

Property	Experiment/DFT	MEAM[a]	BOP
a (Å)*	2.95[a]	2.95	2.92
c (Å)*	4.68[a]	4.69	4.68
E_c (eV/atom)*	−4.87[a]	−4.87	−4.87
C_{11} (GPa)*	176[a]	170	177
C_{12} (GPa)*	87[a]	80	83
C_{13} (GPa)*	68[a]	75	74
C_{33} (GPa)*	191[a]	187	193
C_{44} (GPa)*	51[a]	42	39
$\Delta E_{hcp\to bcc}$ (eV)*	0.07[a]	0.02	0.08
$\Delta E_{hcp\to fcc}$ (eV)*	0.06[a]	0.05	0.11
$\Delta E_{hcp\to sc}$ (eV)	0.41[b]	1.25	0.98
$\Delta E_{hcp\to dia}$ (eV)	1.57[b]	2.26	2.13
V_{Ti} (eV)*	1.55[c]	1.79	1.61
Ti_O (eV)*	2.13[d]	4.53	2.24
Ti_{BO} (eV)*	2.25[d]	3.73	2.27
E^{0001}_{surf} (J/m^2)	2.1, 1.92 (avg)[a]	2.14	1.37
$E^{1\bar{1}00}_{surf}$ (J/m^2)	2.1, 1.92 (avg)[a]	2.15	1.28
$E^{11\bar{2}0}_{surf}$ (J/m^2)	2.1, 1.92 (avg)[a]	2.35	1.63
E^{sf} (J/m^2)	0.290[a]	0.213	0.470
α ($K^{-1}\times10^{-6}$)	8.9[a]	10.2	9.6
C_P (J/K-mol)	25.3[a]	25.8	25.7
T_m (K) (hcp → l)	1737[a]	1706	1660

[a]Reference [38].
[b]Reference [39].
[c]Reference [40].
[d]Reference [41].

IV. RESULTS AND DISCUSSION

A. Titanium and aluminum

Properties of elemental Ti and Al calculated using the BOP are shown in Tables I and II, respectively, along with comparisons to experimental and DFT calculated values, which were used for fitting and validation purposes. Calculations made with MEAM potentials are also shown to illustrate the comparability of the BOP to well-established models of these systems. All fitted properties of Ti and Al are captured with a high degree of accuracy by the BOP. Structural properties such as lattice constants and cohesive energies fall within 1% of their corresponding experimental values. The elastic constants are predicted to within 6 GPa of their actual values with the exception of C_{44} for Ti, which is underestimated by 12 GPa. The MEAM also underestimates this elastic constant by 9 GPa. The BOP correctly predicts HCP and FCC to be the ground state structures of Ti and Al, respectively, with transitions between HCP, FCC, and BCC predicted to within

TABLE II. Calculated properties of Al using the BOP in comparison with experimental and DFT data. Properties calculated with a MEAM potential [42] are also presented for comparison. Properties marked with an asterisk (*) were fitted to, while all others were used for validation. Properties listed are lattice constant (a), cohesive energy (E_c), elastic constants (C_{ij}), structural energy differences (ΔE), vacancy formation energy (V_{Al}), [100] dumbbell interstitial formation energy (Al_i), surface energies (E_{surf}), stacking fault energy (E^{sf}), linear thermal expansion coefficient (α), specific heat (C_P), and melting point (T_m).

Property	Experiment/DFT	MEAM[a]	BOP
a (Å)*	4.03[b]	4.04	4.04
E_c (eV/atom)*	−3.36[a]	−3.36	−3.37
C_{11} (GPa)*	114[a]	114	111
C_{12} (GPa)*	62[a]	62	66
C_{44} (GPa)*	32[a]	32	35
$\Delta E_{fcc\rightarrow bcc}$ (eV)*	0.1[a]	0.12	0.1
$\Delta E_{fcc\rightarrow hcp}$ (eV)*	0.06[a]	0.03	0.02
$\Delta E_{fcc\rightarrow sc}$ (eV)	0.36[c]	0.13	0.41
$\Delta E_{fcc\rightarrow dia}$ (eV)	0.75[c]	0.95	0.28
V_{Al} (eV)*	0.68[a]	0.68	0.69
Al_i (eV)*	2.93[b]	2.49	2.92
E^{100}_{surf} (J/m^2)	1.35[b]	0.848	0.926
E^{110}_{surf} (J/m^2)	1.27[b]	0.948	0.978
E^{111}_{surf} (J/m^2)	1.2[b]	0.629	0.798
E^{sf} (J/m^2)	0.166[a]	0.141	0.095
α (K$^{-1}\times10^{-6}$)	23.5[a]	22.0	26.8
C_P (J/K-mol)	24.7[a]	26.2	23.6
T_m (K)	933[a]	937	1050

[a]Reference [42].
[b]Reference [43].
[c]Reference [40].

TABLE III. Calculated properties of TiC using the BOP in comparison with experimental and DFT data. Properties calculated with a MEAM potential [45] are also presented for comparison. Properties marked with an asterisk (*) were fitted to while all others were used for validation. Properties listed are lattice constant (a), formation energy (E_f), elastic constants (C_{ij}), structural energy differences (ΔE), vacancy formation energies (V_x), tetrahedral interstitial formation energies (X_i), antisite formation energies (X_x), surface energies (E_{surf}), stacking fault energy (E^{sf}), linear thermal expansion coefficient (α), and melting point (T_m).

Property	Experiment/DFT	MEAM[a]	BOP
a (Å)*	4.33[a]	4.42	4.33
E_f (eV/atom)*	−0.78[a]	−0.78	−0.99
C_{11} (GPa)*	513[b]	522	516
C_{12} (GPa)*	106[b]	102	71
C_{44} (GPa)*	178[b]	129	171
$\Delta E_{B1\rightarrow B2}$ (eV)*	1.17[c]	0.58	1.10
$\Delta E_{B1\rightarrow B3}$ (eV)*	0.81[c]	1.1	0.75
$\Delta E_{B1\rightarrow B4}$ (eV)	0.32[c]	0.53	0.72
$\Delta E_{B1\rightarrow B17}$ (eV)	1.06[c]	0.58	1.33
$\Delta E_{B1\rightarrow B81}$ (eV)	0.13[c]	−0.16	0.59
$\Delta E_{B1\rightarrow Bh}$ (eV)	0.71[c]	−0.09	0.70
V_{Ti} (eV)*	7.81[d]	2.96	7.01
V_C (eV)*	−0.5[e]	0.66	−0.75
Ti_i (eV)*	8.19[d]	2.17	8.03
C_i (eV)*	4.09[d]	−2.41	4.08
C_{Ti} (eV)	12.17[d]	5.96	12.95
Ti_C (eV)	6.94[d]	10.02	8.65
E^{100}_{surf} (J/m^2)	1.7[a]	2.91	2.54
E^{110}_{surf} (J/m^2)	3.7[a]	3.76	3.27
E^{111}_{surf} (J/m^2)	4.0[a]	4.05	3.45
E^{sf} (J/m^2)	1.38[f]	1.32	0.76
α (K$^{-1}\times10^{-6}$)	7.7[g]	4.6	5.0
T_m (K)	3340[a]	3000–3500	3500–3600

[a]Reference [45].
[b]Reference [46].
[c]Reference [49].
[d]Reference [50].
[e]Reference [51].
[f]Reference [52].
[g]Reference [53].

tens of meV. Vacancy and self-interstitial formation energies are also predicted to within tens of meV of DFT calculated values. Notably, the BOP does a significantly better job than the MEAM in reproducing interstitial energies.

Properties which were not used in fitting are also relatively well captured by the BOP. Transitions to simple cubic (SC) and diamond cubic (DIA) are predicted to be significantly higher in energy than the corresponding transitions between HCP, FCC, and BCC, as would be expected for metallic systems. Surface energies are generally underestimated, but close-packed surfaces are correctly predicted to be the lowest in energy. Stacking fault energy is overestimated and underestimated for Ti and Al, respectively. Planar defects appear to be one area where the MEAM performs better, most likely due to its inclusion of second nearest neighbors within the cutoff range. Impressively, thermal properties such as the average linear thermal expansion coefficient and specific heat are all predicted to within 15% of their experimentally determined values without any fitting. Both melting points, calculated via the solid-liquid interface method [44], are within 120 K of their actual values, an excellent result for interatomic potentials. Overall, the BOP provides an appropriate model for elemental Ti and Al, and the results are on par with the MEAM, which is commonly used in atomistic modeling of metallic systems. These Ti-Ti and Al-Al interactions were subsequently incorporated into binary (TiC) and ternary (MAX) systems without modification.

B. Titanium carbide

Modeling of TiC includes the previously developed Ti-Ti and C-C interactions along with newly developed Ti-C interactions. Properties of TiC calculated using the BOP are shown in Table III along with comparisons to experimental and DFT calculated values, which were used for fitting and validation purposes. Again, calculations made with a MEAM potential are also shown as a means of benchmarking the BOP's performance. It should be noted that unlike Ti and Al, which have numerous published potentials available for use,

TiC has not been as widely studied, with only two potentials available to date [45,46].

The experimental lattice parameter of TiC is reproduced exactly by the BOP, in contrast to the MEAM which overestimates it by about 0.1 Å. The magnitude of the formation energy is slightly overestimated, but this was deemed acceptable in order to better fit other properties. The elastic constants are reproduced well except for C_{12}, which is underestimated by 35 GPa. This overall result however, represents an improvement over the MEAM as it underestimates C_{44} by nearly 50 GPa. The ground state structure of TiC is rocksalt (B1). To ensure this, the transitions to a number of other common binary structures were calculated: CsCl (B2), zinc blende (B3), wurtzite (B4), PtS (B17), NiAs (B81), and WC (Bh). The BOP predicts all these structures to be higher in energy than the B1 ground state structure. In contrast, the MEAM incorrectly predicts both the B81 and Bh structures to be lower in energy than the B1 structure.

The calculation of point defect energies becomes more complex in nonunary compounds such as TiC, as formation energies are dependent upon the chemical potentials of the constituent species:

$$E^f = E_{\text{def}} - E_{\text{perf}} + \sum_i n_i \mu_i \tag{8}$$

where E_{def} and E_{perf} are the total energies of the defective structure and a defect-free structure, respectively, n_i is the change in the number of atoms of element i, and μ_i is the chemical potential of element i. For simplicity, the chemical potentials of the reference phases (hcp-Ti: -4.87 eV/atom and graphite: -7.37 eV/atom) were adopted. Utilizing Eq. (8), the BOP correctly predicts all vacancy and interstitial formation energies to within 0.8 eV of the values calculated via DFT. This is in contrast to the MEAM, which does not capture any of them with much accuracy. Impressively, both antisite formation energies are also accurately predicted by the BOP to within 2 eV of the DFT calculated values. The MEAM, again, is significantly off in these predictions.

Surface energies are predicted within reason by the BOP, but most importantly, the correct trend is reproduced, with the (100) surface being the lowest in energy and the (111) surface being the highest. Stacking fault energy is underestimated, as priority was placed on point defect properties. Again, the MEAM appears to capture planar defects better than the BOP. Selected thermal properties were calculated, with the average linear coefficient of thermal expansion and melting point being reproduced reasonably well. Overall, the BOP reproduces properties of TiC accurately and can be seen as an improvement over the MEAM due to its inability to capture point defect energies and predict B1 as the ground state structure. The Ti-C interaction was subsequently incorporated into MAX phase systems without further modification. It is important to note that a MAX phase potential, which can also accurately model the corresponding MX phase, is desirable as MX impurity particles are nearly always found in real MAX phase microstructures [47,48].

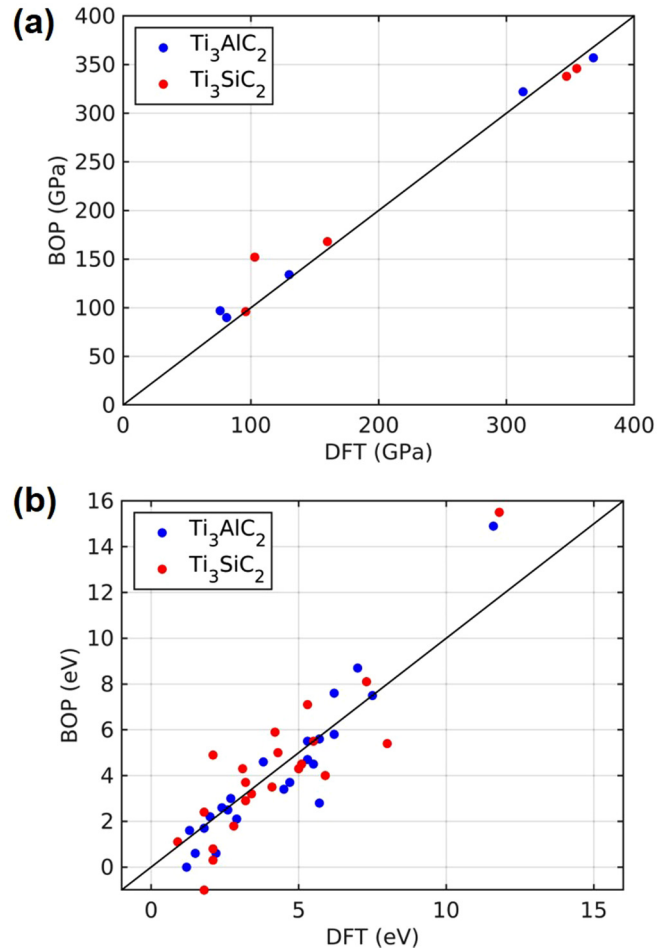

FIG. 3. (a) Elastic constants and (b) point defect formation energies of Ti_3AlC_2 and Ti_3SiC_2 calculated with the BOP plotted against DFT calculated values.

C. Ti_3AlC_2 and Ti_3SiC_2 MAX phases

Extending the BOP to model Ti_3AlC_2 and Ti_3SiC_2 MAX phases includes all previously developed interactions as well as newly developed Ti-Al, Al-C, Ti-Si, and Si-C interactions. Properties of both MAX phases calculated using the BOP are shown in Table IV along with comparisons to experimental and DFT calculated values, which were used for fitting and validation purposes. No additional potentials were available for comparison as was the case for the elemental and binary systems.

The BOP captures the structural properties of both MAX phases well. The lattice constants are calculated to within a few percent of their actual values, despite some accuracy in a for Ti_3AlC_2 being sacrificed to better replicate other properties. The formation energies are predicted to within 0.15 eV, and the β polymorphs are predicted to be higher in energy than the α polymorphs. The only difference between the two polymorphs is a shearing of the A layers relative to the MX layers [1]. Elastic properties are also replicated with a high degree of accuracy, as all elastic constants except C_{13} fall within 15 GPa of their DFT calculated counterparts. This accuracy is visualized in Fig. 3(a), where BOP calculated values are plotted against their respective DFT calculated values.

TABLE IV. Calculated properties of the Ti_3AlC_2 and Ti_3SiC_2 MAX phases using the BOP in comparison with experimental and DFT data. Properties marked with an asterisk (*) were used to fit Ti-A interactions while those marked with a double asterisk (**) were used to fit A-C interactions. All other properties were used for validation. Properties listed are lattice constants (a, c), formation energy (E_f), elastic constants (C_{ij}), structural energy differences (ΔE), vacancy formation energies (V_x), antisite formation energies (X_x), interstitial formation energies (X_i), surface energies (E_{surf}), and linear thermal expansion coefficient (α).

	Ti_3AlC_2		Ti_3SiC_2	
Property	Experiment/DFT	BOP	Experiment/DFT	BOP
a (Å)*	3.07[a]	2.97	3.07[a]	3.08
c (Å)*	18.58[a]	18.60	17.67[a]	17.71
E_f (eV/atom)*	−0.72[b]	−0.85	−0.95[c]	−0.89
$\Delta E_{\alpha\rightarrow\beta}$ (eV/atom)*	0.04[d]	0.01	0.05[d]	0.02
C_{11} (GPa)*	368[e]	357	355[f]	346
C_{12} (GPa)*	81[e]	90	96[f]	96
C_{13} (GPa)*	76[e]	97	103[f]	152
C_{33} (GPa)*	313[e]	322	347[f]	338
C_{44} (GPa)*	130[e]	134	160[f]	168
$V_{Ti_{II}}$ (eV)*	7.5[g]	7.5	7.3[g]	8.1
V_{Ti_I} (eV)*	5.7[g]	5.6	5.5[g]	5.5
V_A (eV)*	2.2[g]	0.6	2.1[g]	0.8
V_C (eV)*	2.9[g]	2.1	2.1[g]	0.3
$A_{Ti_{II}}$ (eV)**	2.7[g]	3.0	4.3[g]	5.0
A_{Ti_I} (eV)**	2.0[g]	2.2	3.2[g]	2.9
Ti_A (eV)	1.2[g]	0.0	1.8[g]	−1.0
$C_{Ti_{II}}$ (eV)	11.6[g]	14.9	11.8[g]	15.5
C_{Ti_I} (eV)	6.2[g]	5.8	5.9[g]	4.0
Ti_C (eV)	6.2[g]	7.6	8.0[g]	5.4
C_A (eV)	3.8[g]	4.6	3.2[g]	3.7
A_C (eV)	5.5[g]	4.5	3.4[g]	3.2
A_a (eV)	5.3[g]	5.5		
A_{b2} (eV)	4.5	3.4	4.2[g]	5.9
A_{c2} (eV)	2.4[g]	2.6	2.1[g]	4.9
Ti_a (eV)	7.0[g]	8.7	5.3[g]	7.1
Ti_{b1} (eV)	5.3[g]	4.7	5.0[g]	4.3
Ti_{b2} (eV)	5.7[g]	2.8	5.1[g]	4.5
Ti_{c1} (eV)	3.8[g]		3.6[g]	
Ti_{c2} (eV)	4.7[g]	3.7	4.1[g]	3.5
C_a (eV)**	2.6[g]	2.5	3.1[g]	4.3
C_{b2} (eV)**	1.3[g]	1.6	0.9[g]	1.1
C_{c1} (eV)**	1.5[g]	0.6	2.8[g]	1.8
C_{c2} (eV)**	1.8[g]	1.7	1.8[g]	2.4
$E_{surf}^{Ti_I-A}$ (J/m^2)	2.1[h]	0.6	2.9[h]	0.9
$E_{surf}^{Ti_I-C}$ (J/m^2)	6.4[h]	5.8	6.3[h]	3.5
$E_{surf}^{Ti_{II}-C}$ (J/m^2)	4.7[h]	3.3	5.1[h]	3.4
α ($K^{-1}x10^{-6}$)	9.1[i]	7.7	9.3[j]	4.9

[a]Reference [1].
[b]Reference [54].
[c]Reference [55].
[d]Reference [56].
[e]Reference [57].
[f]Reference [58].
[g]Reference [59].
[h]Reference [60].
[i]Reference [61].
[j]Reference [62].

The diagonal line represents perfect agreement between the two, and each point does not fall far from this ($R^2 = 0.996$ and 0.975 for Ti_3AlC_2 and Ti_3SiC_2, respectively).

With three constituent elements and four distinct crystallographic sites, 312 MAX phases can exhibit a wide array of point defects. To distinguish between the two different Ti sites in Ti_3AlC_2 and Ti_3SiC_2, the site in the center of the MX block, bonded only to C atoms, is designated Ti_{II}, and the site at the surface of the MX block, bonded to both C and A atoms, is designated Ti_I (Fig. 1). This is done in accordance

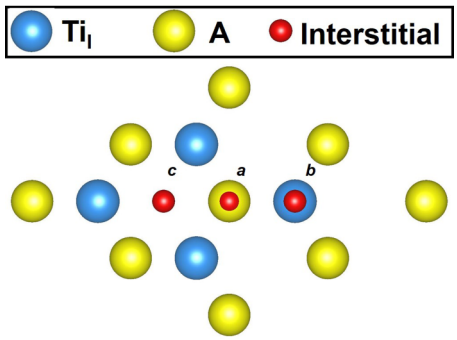

FIG. 4. A schematic showing the locations of interstitial sites within the A layer. Two adjacent layers of Ti_I and A atoms are viewed along the [0001] direction. Interstitials either fall within the layer of A atoms or between the two layers of Ti_I and A atoms.

with the standard laid out by Barsoum [1]. It should be noted that the opposite convention was used by Wang *et al.* [59], from which DFT calculated values of point defect formation energies were taken. In total, four different vacancies and eight different antisites must be considered. In addition to this, there are a number of different interstitial sites available. For simplicity, only those interstitial sites in proximity to the A layer were considered as Ti and C interstitials in the MX layer are fully modeled by the Ti-C interaction and A interstitials in the MX layer have been shown to be exceedingly unlikely [59]. The different interstitial sites present within the A layer are depicted in Fig. 4 and are described similarly to Wang *et al.* [59]. The *a* site occurs between the A and Ti_I planes, the *b* site occurs between the A and Ti_I planes ($b1$) and within the A plane ($b2$), and the *c* site occurs between the A and Ti_I planes ($c1$) and within the A plane ($c2$).

Point defect formation energies were calculated with the BOP according to Eq. (8), again taking the chemical potentials as those of the reference phases (hcp-Ti: −4.87 eV/atom, fcc-Al: −3.36 eV/atom, dia-Si: −4.63 eV/atom, and graphite: −7.37 eV/atom). The four vacancy formation energies are replicated well, with only V_A and V_C in Ti_3SiC_2 being more than 1 eV off. Despite this, the correct trend is maintained in both MAX phases, with $V_{Ti_{II}}$ having the highest formation energy followed by V_{Ti_I} and then V_A and V_C having the lowest. Impressively, all eight antisite formation energies, most of which were not fitted to, are modeled relatively accurately; the majority fall within 1.5 eV of the DFT calculated values. Finally, the numerous interstitial formation energies are also predicted with a good degree of accuracy. The Ti_{c1} site is predicted to be unstable in both MAX phases, decaying into the Ti_{c2} site, but this is not surprising as there remains some disagreement between DFT studies over the stable interstitial sites in MAX phases [59,63,64]. Of particular note, C interstitial formation energies are predicted with a high degree of accuracy. These interstitials are expected to be the most numerous due to their low formation energy. Calculation of the various point defect formation energies is again visualized in Fig. 3(b), with BOP values plotted against DFT calculated values. There are a few outliers, but overall the BOP is able to capture a large number of these point defects accurately ($R^2 = 0.891$ and 0.778 for Ti_3AlC_2 and Ti_3SiC_2, respectively).

Also calculated with the BOP were (0001) surface energies, in which different sets of bonds were broken. The BOP underestimates these energies, but the correct trend is captured. The energy of the surface after breaking Ti_I-A bonds is the lowest, indicating that these are the weakest bonds in the system. Finally, average linear coefficients of thermal expansion were calculated to ensure the BOP can model MAX phases at nonzero temperatures. These values are underestimated but remain within a reasonable range for MAX phases [1]. Overall, the BOP is able to accurately model Ti_3AlC_2 and Ti_3SiC_2, with numerous experimentally determined and DFT calculated properties being replicated. Further validation of the BOP is subsequently presented in the form of large-scale MD simulations, which demonstrate some of the well-documented MAX phase behaviors.

D. Large scale validation

As a complement to the numerous material properties of Ti_3AlC_2 and Ti_3SiC_2 predicted by the BOP, several large-scale tests were performed to serve as further validation that it is an appropriate atomistic model. These include deformation mechanisms in single crystals, high temperature deformation, and KNE behavior.

The deformation of MAX phase single crystals and its anisotropy has been difficult to isolate experimentally from any potential grain boundary effects. However, some work has been done to probe the response of highly-oriented MAX phase grains to uniaxial compression along different axes [65], giving a good approximation to a single crystal response, and recently uniaxial compression of single crystal micropillars was performed [66]. In both cases, when compressed at an angle to the basal planes, a large degree of plastic deformation was observed. This has been ascribed to the presence of 2 slip systems in MAX phases, both contained within the basal planes [1,3]. In contrast, when the basal planes were loaded edge-on, the formation of kink bands was observed to precede any other plastic deformation, as the basal slip systems are not active in this orientation. In both cases, the plastic anisotropy exhibited by MAX phases is clear.

To replicate some aspects of these results, uniaxial compression simulations were performed on fully periodic $10 \times 10 \times 10$ nm^3 blocks of Ti_3AlC_2 and Ti_3SiC_2 utilizing the BOP. The cells were loaded in three different orientations with respect to the basal planes: 45° (angle), 0° (parallel), and 90° (perpendicular). The simulations were carried out at 300 K and with a 10^8 s^{-1} strain rate within the NPT ensemble. The stress-strain curves from these simulations on Ti_3AlC_2 are shown in Fig. 5(a), and the anisotropic response for inelastic deformation and strength, as a function of loading orientation, is obvious. Similar results were obtained for Ti_3SiC_2 [67]. When loaded at an angle to the basal planes, a sawtoothlike (i.e., jerky) curve, typical of materials with active slip systems alternating between nucleation and exhaustion, was generated. There is a high degree of plastic deformation as compressive failure occurred beyond 35% strain. In contrast, when loaded both parallel and perpendicular to the basal planes, a stress-strain curve more typical of brittle materials was

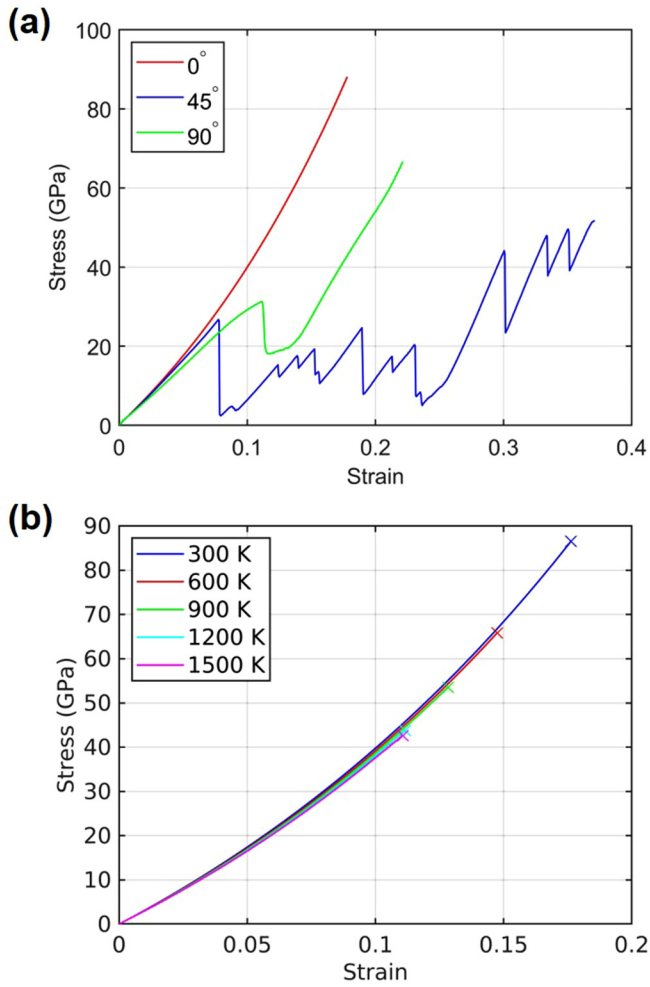

FIG. 5. (a) Stress-strain curves for Ti_3AlC_2 under uniaxial compression in three different orientations with respect to the basal planes. (b) Stress-strain curves for Ti_3AlC_2 under uniaxial compression parallel to the basal planes at various temperatures.

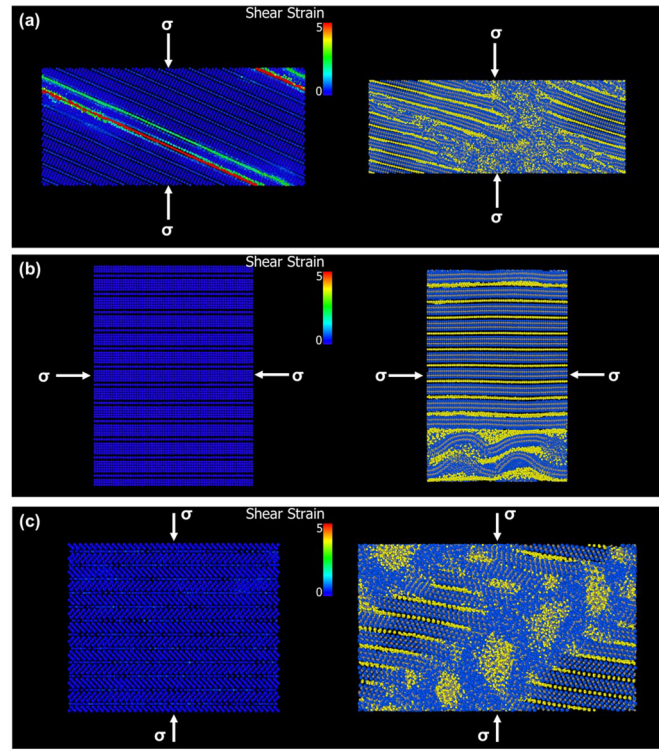

FIG. 6. Snapshots of uniaxial compression simulations on Ti_3AlC_2 immediately before (left) and after (right) compressive failure. Snapshots before are color coded by shear strain, and snapshots after are color coded by atom type (Ti—blue, Al—yellow, C—gray). All three loading orientations are depicted: (a) at an angle to the basal planes, (b) parallel to the basal planes, and (c) perpendicular to the basal planes.

generated. Compressive failure occurred suddenly at a strain around 20%, without any apparent plastic deformation. The noticeable stress drop in the perpendicular case is associated with a rearrangement of the A layers into the β-polymorph structure. This strain-induced transition has been observed experimentally [68,69], but further study is required to fully understand its origin. To better understand the compression results, snapshots of the simulations taken immediately before and after compressive failure are shown in Fig. 6. Snapshots from the simulations performed on Ti_3SiC_2 are available in the Supplemental Material [67]. The snapshots taken before compressive failure are color coded by shear strain to determine if slip occurred. When loaded at an angle to the basal planes, it is clear that a number of slip events occurred prior to failure, and that these were contained within the basal planes [Fig. 6(a)]. This is not the case for parallel and perpendicular loading where no slip events are apparent [Figs. 6(b) and 6(c)]. These results are consistent with MAX phases only having slip systems contained within their basal planes. The snapshots taken after compressive failure are color coded by atom type to provide a better contrast of the layers. When loaded at an angle and perpendicular to the basal planes, failure occurred by shear banding [Figs. 6(a) and 6(c)], as has been observed experimentally [65]. When loaded parallel to the basal planes, sudden failure occurred when the layers began to form buckles, which rapidly propagated throughout the system. In larger systems, these buckles could be precursors to the kink bands observed post mortem in experiments [65,66]. Based on these simulations, the BOP appears to accurately capture the plastic anisotropy of MAX phases and its associated mechanisms. This gives further evidence that the BOP can successfully model MAX phases.

The uniaxial compression simulations, with loading performed parallel to the basal planes were also repeated at regular temperature intervals up to 1500 K. This was done to ensure that no additional nonbasal slip systems become active at high temperatures. While MAX phases are known to undergo a brittle to plastic transition at high temperatures, this is only observed in polycrystalline samples and has therefore been attributed to a temperature dependent grain boundary decohesion stress [1,3]. Observations of decreasing fracture toughness above the transition temperature lend support to this hypothesis [70–72]. The stress-strain curves from these simulations on Ti_3AlC_2 are shown in Fig. 5(b). The curves nearly fall on top of one another, and no additional deformation mechanisms are apparent. Additionally, the strain to failure monotonically decreases with temperature, ruling out

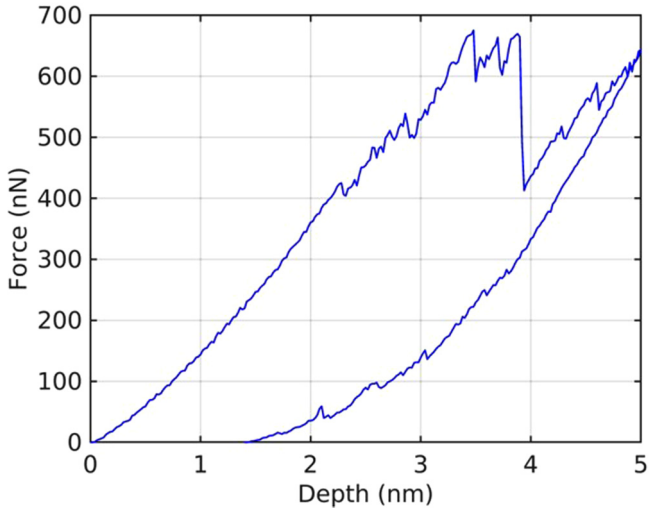

FIG. 7. The force-displacement curve from simulated nanoindentation performed on Ti_3AlC_2.

further plastic deformation. Similar results were obtained for Ti_3SiC_2 [67].

As discussed previously, one of the most well documented phenomena occurring in MAX phases is their KNE behavior. Nanoindentation represents an ideal test to determine if the BOP is able to capture this critical behavior. Therefore nanoindentation was performed on $40 \times 1 \times 60$ nm^3 cells of Ti_3AlC_2 and Ti_3SiC_2, with a 10 nm radius cylindrical indenter and a maximum indentation depth of 5 nm. Indentation was performed parallel to the basal planes (x axis) while periodic boundary conditions were applied to the other two axes. A thin plane of atoms at the base of the indentation direction was held fixed to prevent the cell from moving. Each nanoindentation was performed at 10 K with a constant indentation speed of 1 m/s. The force-displacement curve for the simulated nanoindentation on Ti_3AlC_2 is shown in Fig. 7. The response is initially linear elastic. This is followed by a large pop-in event around an indentation depth of 4 nm. Upon unloading, the cycle ends with residual deformation of around 1.5 nm. The qualitative similarity of this curve with those observed experimentally for MAX phases [15] is striking and provides compelling evidence that the BOP can successfully model KNE behavior. Similar behavior was also predicted for Ti_3SiC_2 [67].

Snapshots from the maximum indentation depth and end of the cycle are shown in Fig. 8 for Ti_3AlC_2. Similar images for Ti_3SiC_2 can be seen in the Supplemental Material [67]. The pop-in event can clearly be associated with the buckling of a series of layers and accompanying delamination between the MX and A layers [Fig. 8(a)]. The buckling appears to be elastic, as upon removal the layers largely recover and delamination disappears [Fig. 8(b)]. These results align well with previous simulations on graphite [13,15], which strongly implicate this type of elastic buckling, i.e., *ripplocations*, in KNE behavior. A more detailed treatment of this mechanism is required to confirm its connection to KNE behavior and will be the focus of future studies.

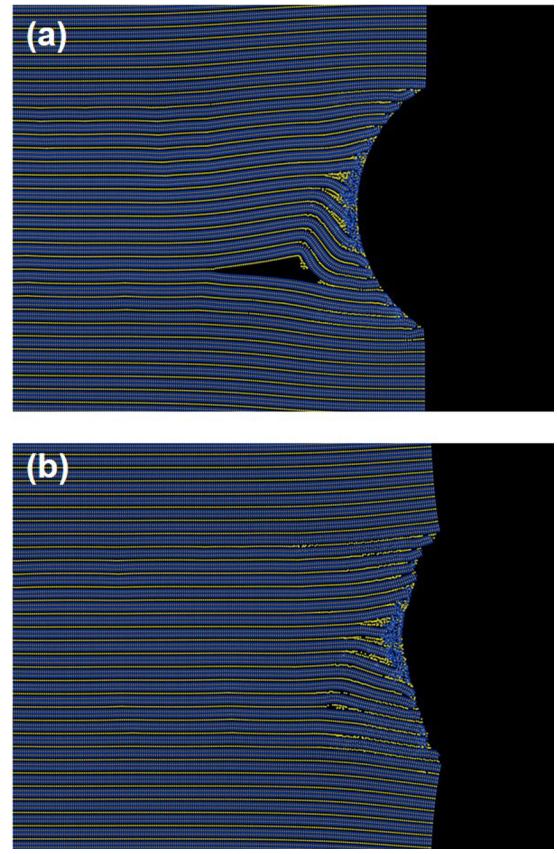

FIG. 8. Snapshots from the simulated nanoindentation performed on Ti_3AlC_2. Atoms are color coded by type (Ti—blue, Al—yellow, C—gray). Snapshots show the maximum indentation depth (a) and residual damage (b).

V. CONCLUSIONS

The bond-order potentials presented herein represent a first highly accurate atomistic model for MAX phases. They have been shown to successfully model Ti_3AlC_2 and Ti_3SiC_2 by replicating a number of structural, elastic, defect, and thermal properties. Additionally, well-documented MAX phase mechanical behaviors such as plastic anisotropy, high temperature deformation, and kinking nonlinear elasticity are well captured. This now provides an invaluable tool for future studies into some of the elusive atomic-scale mechanisms which govern many unique MAX phase properties. Importantly as well, the fitting procedure used to generate the bond-order potentials is highly transferable due to its stepwise nature. It should be applicable to numerous other MAX phases, provided the appropriate data is available for fitting.

ACKNOWLEDGMENTS

G.P. acknowledges support through the CoorsTek Graduate Fellowship Program at Colorado School of Mines. G.J.T. is grateful for financial support through ARO Grant No. W911NF1910389. Work reported here was run on hardware supported by the High Performance Computing group at Colorado School of Mines. The authors declare no competing interests.

APPENDIX: BOP INTERACTION PARAMETERS

Finalized parameters for the Ti-Al-C and Ti-Si-C systems are presented below in Tables V, VI, and VII.

TABLE V. BOP interaction parameters for the elemental interactions in the Ti-Al-C and Ti-Si-C systems. Si-Si and C-C parameters were previously developed [21]. The R parameter for Si-Si has been adjusted from its original value to allow for Si-Si interactions in the MAX phase structure.

Parameter	Ti-Ti	Al-Al	Si-Si	C-C
λ_3	0.590960	0.363640	0.000000	0.000000
γ	0.001963	0.027500	0.092530	0.112330
c	1.356500	2.997400	1.136810	181.910000
d	0.230100	0.786240	0.633970	6.284330
h	−0.904680	−0.265140	−0.335000	−0.555600
λ_2	1.367849	1.277747	1.665910	1.930901
B	184.973776	84.832556	361.557047	175.426651
λ_1	1.940020	2.135627	2.615479	4.184262
A	540.866546	374.189252	1899.385778	2019.844901
R	3.580900	3.744100	3.400000	2.000000
D	0.302900	0.297020	0.150000	0.150000

TABLE VI. BOP Interaction Parameters for the binary interactions in the Ti-Al-C and Ti-Si-C systems.

Parameter	Ti-C	Ti-Al	Ti-Si	Al-C	Si-C
$\lambda_3(i,i,j)$	−0.027320	−1.140697	0.145246	0.967367	0.455978
$\lambda_3(i,j,j)$	−1.895700	0.736096	1.653831	0.059156	0.949861
$\lambda_3(i,j,i)$	3.056400	0.205490	0.602082	1.022832	0.148210
$\lambda_3(j,j,i)$	−0.054821	0.728086	0.580472	0.047363	0.399028
γ	0.000185	0.000555	0.059380	0.132625	0.022729
c	103.150000	4.373809	0.647034	31.323255	119.017694
d	1.861400	0.459645	0.588344	3.460896	4.873285
h	0.030954	−0.100655	1.061262	−0.226229	0.279374
λ_2	1.629410	2.384231	1.525709	1.047526	2.499482
B	389.426084	1365.093317	230.770049	54.152110	1752.384773
λ_1	1.940953	3.187173	2.970786	2.101689	4.496459
A	593.352371	7557.640826	3790.763031	151.119263	46383.947502
R	2.731200	3.501812	3.256477	3.001438	2.960379
D	0.187530	0.200103	0.297824	0.250128	0.251126

TABLE VII. Additional ternary interaction parameters for the Ti-Al-C and Ti-Si-C systems.

Parameter	Value
λ_3(Ti, C, Al)	4.553363
λ_3(Ti, Al, C)	0.410875
λ_3(Al, C, Ti)	0.221140
λ_3(Ti, C, Si)	0.651124
λ_3(Ti, Si, C)	0.381585
λ_3(Si, C, Ti)	0.770368

[1] M. W. Barsoum, *MAX Phases: Properties of Machinable Ternary Carbides and Nitrides* (Wiley-VCH, Weinheim, Germany, 2013).

[2] M. W. Barsoum, The $M_{N+1}AX_N$ phases: A new class of solids: Thermodynamically stable nanolaminates, Prog. Solid State Chem. **28**, 201 (2000).

[3] M. W. Barsoum and M. Radovic, Elastic and mechanical properties of the max phases, Annu. Rev. Mater. Res. **41**, 195 (2011).

[4] M. Radovic and M. W. Barsoum, Max phases: bridging the gap between metals and ceramics, American Ceramics Society Bulletin **92**, 20 (2013).

[5] M. W. Barsoum and T. El-Raghy, The max phases: Unique new carbide and nitride materials: Ternary ceramics turn out to be surprisingly soft and machinable, yet also heat-tolerant, strong and lightweight, Am. Sci. **89**, 334 (2001).

[6] C. Walter, C. Martinez, T. El-Raghy, and J. M. Schneider, Towards large area max phase coatings on steel, Steel Research International **76**, 225 (2005).

[7] J. Frodelius, M. Sonestedt, S. Björklund, J.-P. Palmquist, K. Stiller, H. Högberg, and L. Hultman, Ti_2AlC coatings deposited by high velocity oxy-fuel spraying, Surf. Coat. Technol. **202**, 5976 (2008).

[8] H. L. Tuller, M. A. Spears, and R. Micak, Stable electrical contact for silicon carbide devices (2003), US Patent No. 6,544,674.

[9] E. Hoffman, D. Vinson, R. Sindelar, D. Tallman, G. Kohse, and M. Barsoum, Max phase carbides and nitrides: Properties for future nuclear power plant in-core applications and neutron transmutation analysis, Nucl. Eng. Des. **244**, 17 (2012).

[10] M. Barsoum, T. Zhen, S. Kalidindi, M. Radovic, and A. Murugaiah, Fully reversible, dislocation-based compressive deformation of Ti_3SiC_2 to 1 gpa, Nat. Mater. **2**, 107 (2003).

[11] B. T. Kelly, *Physics of Graphite* (Springer, London, 1981).

[12] I. Bell, C. Wilson, A. McLaren, and M. Etheridge, Kinks in mica: role of dislocations and (001) cleavage, Tectonophysics **127**, 49 (1986).

[13] J. Gruber, A. C. Lang, J. Griggs, M. L. Taheri, G. J. Tucker, and M. W. Barsoum, Evidence for bulk ripplocations in layered solids, Sci. Rep. **6**, 33451 (2016).

[14] M. Barsoum and G. Tucker, Deformation of layered solids: ripplocations not basal dislocations, Scr. Mater. **139**, 166 (2017).

[15] J. Griggs, A. C. Lang, J. Gruber, G. Tucker, M. Taheri, and M. Barsoum, Spherical nanoindentation, modeling and transmission electron microscopy evidence for ripplocations in Ti_3SiC_2, Acta Mater. **131**, 141 (2017).

[16] M. W. Barsoum, X. Zhao, S. Shanazarov, A. Romanchuk, S. Koumlis, S. J. Pagano, L. Lamberson, and G. J. Tucker, Ripplocations: A universal deformation mechanism in layered solids, Phys. Rev. Mater. **3**, 013602 (2019).

[17] D. J. Tallman, L. He, J. Gan, N. C. El'ad, E. N. Hoffman, and M. W. Barsoum, Effects of neutron irradiation of Ti_3SiC_2 and Ti_3AlC_2 in the 121–1085 °C temperature range, J. Nucl. Mater. **484**, 120 (2017).

[18] C. Ang, S. Zinkle, C. Shih, C. Silva, N. Cetiner, and Y. Katoh, Phase stability, swelling, microstructure and strength of Ti_3SiC_2-TiC ceramics after low dose neutron irradiation, J. Nucl. Mater. **483**, 44 (2017).

[19] P. Liu, X. Han, D. Sun, and Q. Wang, Development and application of a ternary ti-al-n interatomic potential for $Ti_2AlN/TiAl$ composite, J. Alloys Compd. **745**, 63 (2018).

[20] J. Tersoff, New empirical approach for the structure and energy of covalent systems, Phys. Rev. B **37**, 6991 (1988).

[21] P. Erhart and K. Albe, Analytical potential for atomistic simulations of silicon, carbon, and silicon carbide, Phys. Rev. B **71**, 035211 (2005).

[22] T. Kumagai, S. Izumi, S. Hara, and S. Sakai, Development of bond-order potentials that can reproduce the elastic constants and melting point of silicon for classical molecular dynamics simulation, Comput. Mater. Sci. **39**, 457 (2007).

[23] K. Albe, K. Nordlund, and R. S. Averback, Modeling the metal-semiconductor interaction: Analytical bond-order potential for platinum-carbon, Phys. Rev. B **65**, 195124 (2002).

[24] N. Juslin, P. Erhart, P. Träskelin, J. Nord, K. O. E. Henriksson, K. Nordlund, E. Salonen, and K. Albe, Analytical interatomic potential for modeling nonequilibrium processes in the W–C–H system, J. Appl. Phys. **98**, 123520 (2005).

[25] M. Müller, P. Erhart, and K. Albe, Analytic bond-order potential for bcc and fcc ironâcomparison with established embedded-atom method potentials, J. Phys.: Condens. Matter **19**, 326220 (2007).

[26] K. O. E. Henriksson, C. Björkas, and K. Nordlund, Atomistic simulations of stainless steels: a many-body potential for the Fe-Cr-C system, J. Phys.: Condens. Matter **25**, 445401 (2013).

[27] K. Albe, K. Nordlund, J. Nord, and A. Kuronen, Modeling of compound semiconductors: Analytical bond-order potential for Ga, As, and GaAs, Phys. Rev. B **66**, 035205 (2002).

[28] J. Nord, K. Albe, P. Erhart, and K. Nordlund, Modelling of compound semiconductors: analytical bond-order potential for gallium, nitrogen and gallium nitride, J. Phys.: Condens. Matter **15**, 5649 (2003).

[29] P. Erhart, N. Juslin, O. Goy, K. Nordlund, R. Müller, and K. Albe, Analytic bond-order potential for atomistic simulations of zinc oxide, J. Phys.: Condens. Matter **18**, 6585 (2006).

[30] D. A. Murdick, X. W. Zhou, H. N. G. Wadley, D. Nguyen-Manh, R. Drautz, and D. G. Pettifor, Analytic bond-order potential for the gallium arsenide system, Phys. Rev. B **73**, 045206 (2006).

[31] D. K. Ward, X. W. Zhou, B. M. Wong, F. P. Doty, and J. A. Zimmerman, Analytical bond-order potential for the cadmium telluride binary system, Phys. Rev. B **85**, 115206 (2012).

[32] K. Chenoweth, A. C. Van Duin, and W. A. Goddard, Reaxff reactive force field for molecular dynamics simulations of hydrocarbon oxidation, J. Phys. Chem. A **112**, 1040 (2008).

[33] T. Liang, T.-R. Shan, Y.-T. Cheng, B. D. Devine, M. Noordhoek, Y. Li, Z. Lu, S. R. Phillpot, and S. B. Sinnott, Classical atomistic simulations of surfaces and heterogeneous interfaces with the charge-optimized many body (comb) potentials, Mater. Sci. Eng., R **74**, 255 (2013).

[34] B.-J. Lee and M. I. Baskes, Second nearest-neighbor modified embedded-atom-method potential, Phys. Rev. B **62**, 8564 (2000).

[35] J. C. Lagarias, J. A. Reeds, M. H. Wright, and P. E. Wright, Convergence properties of the nelder–mead simplex method in low dimensions, SIAM J. Optim. **9**, 112 (1998).

[36] S. Plimpton, Fast parallel algorithms for short-range molecular dynamics, J. Comput. Phys. **117**, 1 (1995).

[37] A. Stukowski, Visualization and analysis of atomistic simulation data with ovito–the open visualization tool, Modell. Simul. Mater. Sci. Eng. **18**, 015012 (2009).

[38] Y.-M. Kim, B.-J. Lee, and M. I. Baskes, Modified embedded-atom method interatomic potentials for ti and zr, Phys. Rev. B **74**, 014101 (2006).

[39] M. Mendelev, T. Underwood, and G. Ackland, Development of an interatomic potential for the simulation of defects, plasticity, and phase transformations in titanium, J. Chem. Phys. **145**, 154102 (2016).

[40] R. R. Zope and Y. Mishin, Interatomic potentials for atomistic simulations of the ti-al system, Phys. Rev. B **68**, 024102 (2003).

[41] M. Baskes and R. Johnson, Modified embedded atom potentials for hcp metals, Modell. Simul. Mater. Sci. Eng. **2**, 147 (1994).

[42] B.-J. Lee, J.-H. Shim, and M. I. Baskes, Semiempirical atomic potentials for the fcc metals Cu, Ag, Au, Ni, Pd, Pt, Al, and Pb based on first and second nearest-neighbor modified embedded atom method, Phys. Rev. B **68**, 144112 (2003).

[43] M. Mendelev, M. Kramer, C. A. Becker, and M. Asta, Analysis of semi-empirical interatomic potentials appropriate for simulation of crystalline and liquid al and cu, Philos. Mag. **88**, 1723 (2008).

[44] J. R. Morris, C. Z. Wang, K. M. Ho, and C. T. Chan, Melting line of aluminum from simulations of coexisting phases, Phys. Rev. B **49**, 3109 (1994).

[45] Y.-M. Kim and B.-J. Lee, Modified embedded-atom method interatomic potentials for the Ti–C and Ti–N binary systems, Acta Mater. **56**, 3481 (2008).

[46] T. Liang, M. Ashton, K. Choudhary, D. Zhang, A. F. Fonseca, B. C. Revard, R. G. Hennig, S. R. Phillpot, and S. B. Sinnott, Properties of Ti/TiC interfaces from molecular dynamics simulations, J. Phys. Chem. C **120**, 12530 (2016).

[47] M. Barsoum and T. El-Raghy, Synthesis and characterization of a remarkable ceramic: Ti_3SiC_2, J. Am. Ceram. Soc. **79**, 1953 (1996).

[48] N. V. Tzenov and M. W. Barsoum, Synthesis and characterization of Ti_3AlC_2, J. Am. Ceram. Soc. **83**, 825 (2000).

[49] E. R. Margine, A. N. Kolmogorov, M. Reese, M. Mrovec, C. Elsässer, B. Meyer, R. Drautz, and D. G. Pettifor, Development of orthogonal tight-binding models for Ti-C and Ti-N systems, Phys. Rev. B **84**, 155120 (2011).

[50] W. Sun, H. Ehteshami, and P. A. Korzhavyi, Structure and energy of point defects in tic: An ab initio study, Phys. Rev. B **91**, 134111 (2015).

[51] M. Råsander, H. W. Hugosson, and A. Delin, Density functional study of carbon vacancies in titanium carbide, J. Phys.: Condens. Matter **30**, 015702 (2017).

[52] H. Ding, X. Fan, K. Chu, X. Zhang, and X. Liu, The influence of carbon vacancies on the stacking fault energy of tic, J. Eur. Ceram. Soc. **34**, 1893 (2014).

[53] M. Bauccio, *ASM Engineered Materials Reference Book* (CRC, Materials Park, Ohio, 1994).

[54] V. Witusiewicz, B. Hallstedt, A. Bondar, U. Hecht, S. Sleptsov, and T. Y. Velikanova, Thermodynamic description of the al–c–ti system, J. Alloys Compd. **623**, 480 (2015).

[55] Y. Du, J. C. Schuster, H. J. Seifert, and F. Aldinger, Experimental investigation and thermodynamic calculation of the titanium–silicon–carbon system, J. Am. Ceram. Soc. **83**, 197 (2000).

[56] V. J. Keast, S. Harris, and D. K. Smith, Prediction of the stability of the $M_{n+1}AX_n$ phases from first principles, Phys. Rev. B **80**, 214113 (2009).

[57] X. He, Y. Bai, C. Zhu, Y. Sun, M. Li, and M. Barsoum, General trends in the structural, electronic and elastic properties of the M_3AlC_2 phases (M = transition metal): A first-principle study, Comput. Mater. Sci. **49**, 691 (2010).

[58] J.-Y. Wang and Y.-C. Zhou, Polymorphism of ti 3 sic 2 ceramic: first-principles investigations, Phys. Rev. B **69**, 144108 (2004).

[59] J. Wang, B. Liu, J. Wang, and Y. Zhou, Theoretical investigation of thermodynamic stability and mobility of the intrinsic point defects in ti 3 ac 2 (a= si, al), Phys. Chem. Chem. Phys. **17**, 8927 (2015).

[60] H. Zhang and S. Wang, First-principles study of Ti_3AC_2 (A = Si, Al)(0 0 1) surfaces, Acta Mater. **55**, 4645 (2007).

[61] W.-K. Pang, I.-M. Low, and Z.-M. Sun, In situ high-temperature diffraction study of the thermal dissociation of Ti_3AlC_2 in vacuum, J. Am. Ceram. Soc. **93**, 2871 (2010).

[62] T. Scabarozi, S. Amini, O. Leaffer, A. Ganguly, S. Gupta, W. Tambussi, S. Clipper, l. J. Spanier, M. Barsoum, J. Hettinger *et al.*, Thermal expansion of select $M_{n+1}AX_n$ (M = early transition metal, $A = A$ group element, $X = C$ or N)) phases measured by high temperature x-ray diffraction and dilatometry, J. Appl. Phys. **105**, 013543 (2009).

[63] S. C. Middleburgh, G. R. Lumpkin, and D. Riley, Accommodation, accumulation, and migration of defects in Ti_3SiC_2 and Ti_3AlC_2 MAX phases, J. Am. Ceram. Soc. **96**, 3196 (2013).

[64] S. Zhao, J. Xue, Y. Wang, and Q. Huang, Ab initio study of irradiation tolerance for different $M_{n+1}AX_n$ phases: Ti_3SiC_2 and Ti_3AlC_2, J. Appl. Phys. **115**, 023503 (2014).

[65] M. Barsoum and T. El-Raghy, Room-temperature ductile carbides, Metall. Mater. Trans. A **30**, 363 (1999).

[66] M. Higashi, S. Momono, K. Kishida, N. L. Okamoto, and H. Inui, Anisotropic plastic deformation of single crystals of the max phase compound Ti_3SiC_2 investigated by micropillar compression, Acta Mater. **161**, 161 (2018).

[67] See Supplemental Material at http://link.aps.org/supplemental/10.1103/PhysRevB.100.214114 for Ti_3SiC_2 results.

[68] L. Farber, I. Levin, M. Barsoum, T. El-Raghy, and T. Tzenov, High-resolution transmission electron microscopy of some Tin + 1AX$_n$ compounds (n = 1, 2; A = Al or Si; X = C or N), J. Appl. Phys. **86**, 2540 (1999).

[69] Z. Wang, C. Zha, and M. Barsoum, Compressibility and pressure-induced phase transformation of Ti_2GeC_2, Appl. Phys. Lett. **85**, 3453 (2004).

[70] D. Chen, K. Shirato, M. W. Barsoum, T. El-Raghy, and R. O. Ritchie, Cyclic fatigue-crack growth and fracture properties in Ti_3SiC_2 ceramics at elevated temperatures, J. Am. Ceram. Soc. **84**, 2914 (2001).

[71] D. Wan, F. Meng, Y. Zhou, Y. Bao, and J. Chen, Effect of grain size, notch width, and testing temperature on the fracture toughness of $Ti_3Si(Al)C_2$ and Ti_3AlC_2 using the chevron-notched beam (cnb) method, J. Eur. Ceram. Soc. **28**, 663 (2008).

[72] W. Tian, Z. Sun, H. Hashimoto, and Y. Du, Compressive deformation behavior of ternary compound Cr_2AlC, J. Mater. Sci. **44**, 102 (2009).